Coarse-grained molecular dynamics simulations of the tensile behavior of a thermosetting polymer

Shaorui Yang[1] and Jianmin Qu[1,2,*]

[1]*Department Mechanical Engineering, Northwestern University, Evanston, Illinois 60208, USA*
[2]*Department of Civil and Environmental Engineering, Northwestern University, Evanston, Illinois 60208, USA*

Using a previously developed coarse-grained model, we conducted large-scale ($\sim 85 \times 85 \times 85$ nm^3) molecular dynamics simulations of uniaxial-strain deformation to study the tensile behavior of an epoxy molding compound, epoxy phenol novolacs (EPN) bisphenol A (BPA). Under the uniaxial-strain deformation, the material is found to exhibit cavity nucleation and growth, followed by stretching of the ligaments separated by the cavities, until the ultimate failure through ligament scissions. The nucleation sites of cavities are rather random and the subsequent cavity growth accounts for much (87%) of the volumetric change during the uniaxial-strain deformation. Ultimate failure of the materials occurs when the cavity volume fraction reaches $\sim 60\%$. During the entire deformation process, polymer strands in the network are continuously extended to their linear states and broken in the postyielding strain hardening stage. When most of the strands are stretched to their taut configurations, rapid scission of a large number of strands occurs within a small strain increment, which eventually leads to fracture. Finally, through extensive numerical simulations of various loading conditions in addition to uniaxial strain, we find that yielding of the EPN-BPA can be described by the pressure-modified von Mises yield criterion.

PACS number(s): 61.41.+e

I. INTRODUCTION

Epoxy-based thermosets have found numerous applications as adhesives, molding compounds, and binders for composites in electronic packaging, automotive manufacturing, and aerospace industries. Fracture of epoxies has long been an issue of intensive study. Despite their macroscopically brittle behavior, there has been reported evidence of localized plastic deformation in the literature for epoxy-based thermosets. For example, Morgan and O'Neal [1] observed that epoxy films deform and fail by a crazing process, a predominant toughening mechanism considered to occur only in thermoplastics. The crazing phenomenon was also reported for a high-performance resin (AB-benzocyclobutene-maleimide) [2,3]. Similar to crazing but lacking the distinct fibrils, dilatation bands were found to form within a series of moderately cross-linked thermosets and enhanced by toughening particles [3,4]. Such experimental observations cannot be explained by the brittle nature of epoxy thermosets observed macroscopically. Therefore, there is a need to gain a comprehensive understanding of the conditions and mechanisms of the initiation, growth, and eventual failure of such localized plastic deformations at the submicron scale. However, direct tracking and measuring of these submicron physical processes are extremely difficult, if not impossible.

Molecular dynamics (MD) simulations have been used to successfully simulate the mechanical behaviors of polymers. For instance, yielding [5,6] and strain hardening [7,8] have been investigated for amorphous polymer glasses using coarse-grained (CG) models. In other studies, researchers have examined the nucleation, growth, microstructure, and failure of crazes formed in glassy thermoplastics [9,10] and obtained fracture-related properties based on MD simulation results [11]. Unlike thermoplastic polymers, which have been extensively investigated, results on thermosets are rather

limited, due to the complexities associated with modeling the chemically cross-linked network structure inherent to this type of material. Highly cross-linked polymer networks were studied in [12–14] using coarse-grained molecular dynamics (CGMD) simulations to understand the interfacial fracture between the polymer networks and a solid substrate. The effects of monomer functionality, degree of curing, and interfacial bond density were also examined. However, these works focused on debonding of polymer networks from the confining walls rather than the cohesive fracture within the bulk material. Thus, the detailed microstructure of the large plastic deformation within the polymer was not analyzed. Panico *et al.* [15] simulated the tensile failure of glassy polymers and discussed the different mechanical behavior between thermoplastics and thermosets and concluded that chemical cross-linking embrittles the polymer. In all these aforementioned studies, the CG models are based on nondimensional parameters. Consequently, their results do not provide physically meaningful quantitative information, for example, the length scale and stress magnitude.

In our earlier work [16], a fully atomistic MD investigation provided an accurate prediction of key thermomechanical properties of a commercially important epoxy molding compound epoxy phenol novolacs (EPN) bisphenol A (BPA). Subsequently, a CG model for the EPN-BPA was developed [17]. In this work, the CG model developed in [17] will be used to conduct large-scale simulations of the EPN-BPA to understand its tensile deformation and failure mechanism. Experimental observations of the crazes and dilatation bands [1–4] indicate that the localized plastic deformations in epoxies occur within a narrow band of a few microns or less (several hundred nanometers). While including the entire crack tip is still not realistic even in our CG model, the material volume ($\sim 85 \times 85 \times 85$ nm^3) simulated in the current study is approaching the length scale of a crack-tip opening and can thus serve as a representative volume to study cavity nucleation and growth and ligament scission. The rest of the paper is organized as follows. In Sec. II we describe the CG
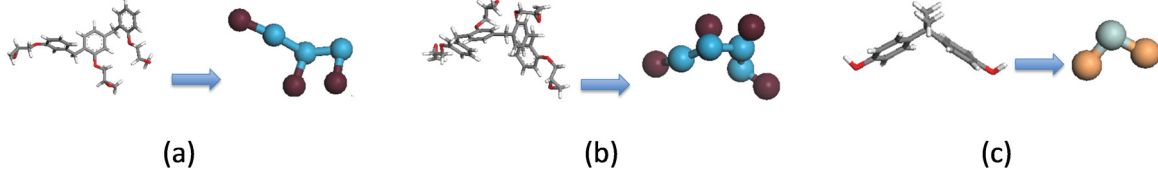
―――――――
*j-qu@northwestern.edu

FIG. 1. (Color online) Bead-connector representations of monomers: (a) EPN 3-mer, (b) EPN 4-mer, and (c) BPA. (a) and (b) Dark gray (brown) beads are reactive beads on epoxy monomers and (c) two-sided (yellow) beads are reactive beads on hardener monomers.

molecular model used and the methodology of conducting nonequilibrium CGMD simulations. Results of the simulations are presented in Sec. III with a detailed discussion of the interpretations of the simulation results. A summary and concluding remarks are given in Sec. IV.

II. SIMULATION METHOD

A. Material and coarse-grained model

The model material studied in this paper is an EPN-BPA epoxy system composed of EPN as epoxy monomer and BPA as the cross-linking agent. The molecular structures of this material and its curing reaction mechanisms can be found in [16]. The CG model developed in [17] will be used. For completeness, a brief overview of the CG model is repeated here.

In this CG model, the monomers are represented by beads connected by chains that maintain similar geometry as their realistic atomistic configurations. Different monomer structures are mapped onto different bead-chain structures (see Fig. 1). Certain groups of atoms on epoxy monomers (EPN 3-mer and EPN 4-mer) are mapped onto reactive beads as are the hardener monomers. During MD simulated cross-linking process, bonds are continuously introduced between these two types of beads.

For simplicity, it is assumed that all the beads have the same effective mass M, which will need to be determined together with other parameters in the interbead potential. The nonbonded interactions between beads are described by the Lennard-Jones (LJ) potential

$$U_{LJ}(r) = 4\varepsilon\left[\left(\frac{\sigma}{r}\right)^{12} - \left(\frac{\sigma}{r}\right)^6\right], \tag{1}$$

where ε and σ represent the potential-well depth and diameter, respectively. They are assumed to be the same for all beads. The truncation distance for the LJ potential is set equal to 2.5σ. In our computations, the LJ interactions are invoked only for beads that are separated by at least three bonds.

The bonded interactions between beads are described by a quartic function of the interbead distance r and a purely repulsive LJ function, with a cutoff

at $2^{1/6}\sigma$,

$$U_b(r) = U_0 + k_4(r-r_c)^2(r-b_1-r_c)(r-b_2-r_c)H(r_c-r)$$
$$+ 4\varepsilon\left[\left(\frac{\sigma}{r}\right)^{12} - \left(\frac{\sigma}{r}\right)^6 + \frac{1}{4}\right]H(2^{1/6}\sigma-r)H(r_c-r), \tag{2}$$

where $H(x)$ is the Heaviside step function, $k_4 = 1434.3\varepsilon/\sigma^4$, $b_1 = -0.7589\sigma$, $b_2 = 0$, and $U_0 = 67.2234\varepsilon$ [18]. The bond extension cutoff r_c will be among the parameters to be fitted. At r_c, the potential is smoothly truncated and the bond is removed from the system (bond breakage). Meanwhile, the LJ pair potential given by (1) is turned on between the aforebonded pair.

The angle bending interaction is described by a quadratic function of the bond angle

$$U_a^{(i)}(\theta) = k_\theta^{(i)}\left(\theta - \theta_0^{(i)}\right)^2, \tag{3}$$

where $\theta_0^{(i)}$ is the equilibrium bond angle. In this work, three types of bond angles are defined. The angle formed by the three beads in a BPA monomer is called type 1, whose equilibrium angle is assumed to be $\theta_0^{(1)} = 100°$. The angle formed by a reactive bead in an EPN monomer and a reactive bead in a BPA monomer is called type 2, whose equilibrium angle is assumed to be $\theta_0^{(2)} = 180°$. All other angles formed by beads within each EPN monomer are called type 3, whose equilibrium angle is assumed to be $\theta_0^{(3)} = 180°$. These assumptions on the equilibrium angles are made based on the geometry of the atomistic configurations of the monomers (see Fig. 1). The prefactor $k_\theta^{(i)}$, with $i = 1,2,3$, will be determined through the parameter optimization procedure.

In all, there are seven adjustable parameters in the interbead potentials given by (1)–(3), namely, M, ε, σ, r_c, $k_\theta^{(1)}$, $k_\theta^{(2)}$, and $k_\theta^{(2)}$, that need to be determined. This task is accomplished by using the particle swarm optimization method [19] to iteratively reduce the difference between the CG model simulated and fully atomistic model simulated material properties such as density, glass transition temperature, and elastic constants for non-cross-linked and 90% cross-linked epoxy molding compound. Their optimized values are listed in Table I. Details of the optimization algorithm and implementation are given in [17].

TABLE I. Optimized force-field parameters.

M (g/mol)	ε (kcal/mol)	σ (Å)	k_4 (kcal/mol Å^4)	r_c (Å)	b_1 (Å)	b_2 (Å)	U_0 (kcal/mol)	$k_\theta^{(1)}$ (kcal/mol-rad^2)	$k_\theta^{(2)}$	$k_\theta^{(3)}$
55.565	1.519	4.383	5.901	5.887	−3.326	0.0	102.082	2.395	2.899	0.613

B. Cross-linking and tensile simulation

To build a simulation cell, a group of CG beads representing epoxy and hardener monomers is randomly seeded in a cubic simulation cell with periodic boundary conditions in all three orthogonal directions. The number of different types of monomers obeys the stoichiometric ratio 2:3:9 for 3-mer:4-mer:BPA. The assembly of beads in the simulation cell is then equilibrated under an *NPT* ensemble at a temperature of 500 K with a time step of 5 fs for 1×10^6 steps. Thereafter, a dynamic cross-linking process is conducted during the constant-temperature and -pressure MD simulation. In this process, a bond is formed between an EPN reactive bead and a BPA reactive bead when their separation is less than 1.3σ. Note that the formation of each new bond increases the system energy by a certain amount. To avoid a drastic change of the system energy, the number of bonds formed during each simulation time step should be kept low. To this end, we assign a probability of 0.01 for the bond formation. In other words, at each simulation time step, a bond is formed on only one pair of EPN and BPA beads out of 100 pairs that are within a distance of 1.3σ. Further, we allow such bond formation to take place once every ten MD time steps. At this rate, the conversion degree of 90% typically takes 400 000–500 000 steps. Due to the three-dimensional periodic nature of the simulation cell, the cross-linked network actually extends to infinity in all three directions. After the dynamic cross-linking reaches the desired conversion degree, the simulation cell is quenched from 500 to 300 K at 2.2×10^{10} K/s, followed by 1×10^6 steps of the *NPT* simulation at 300 K to reach the equilibrium density of 1.183 g/cm^3. The results presented in the present paper are based on a simulation cell that contains 7 834 220 beads, corresponding to its size of $\sim 85 \times 85 \times 85$ nm^3 at room temperature equilibrium.

The next step is to simulate the tensile behavior. This is accomplished by subjecting the cross-linked and equilibrated polymer network to a tensile deformation at 300 K, which is below the glass transition temperature of 400 K for this material, according to our previous coarse-grained MD calculations [17]. The deformation is induced by elongating the simulation cell along the loading axis with a strain rate of 10^8 s^{-1}, while keeping the other two perpendicular directions undeformed, effectively creating a unidirectional strain. This strain rate is obviously much higher than that used in quasistatic loading in realistic laboratory tests. Therefore, the results given in the remainder of this paper must be interpreted with this high strain rate in mind. This scheme of deformation provides a triaxial stress state with strong dilatation component and thus promotes cavity nucleation and growth. Such high hydrostatic stresses are often found in crazes and dilatational bands.

III. RESULTS AND DISCUSSION

A. Stress-strain curve

Figure 2 shows a stress-strain curve under the uniaxial strain condition described in the previous section. It is seen that at about 7% strain, the material reaches its yield strength of $\sim$298 MPa. After yielding, the stress immediately relaxes down to $\sim$110 MPa. This drastic relaxation is due to cavity nucleation as shown in the snapshot in Fig. 3(a), where beads
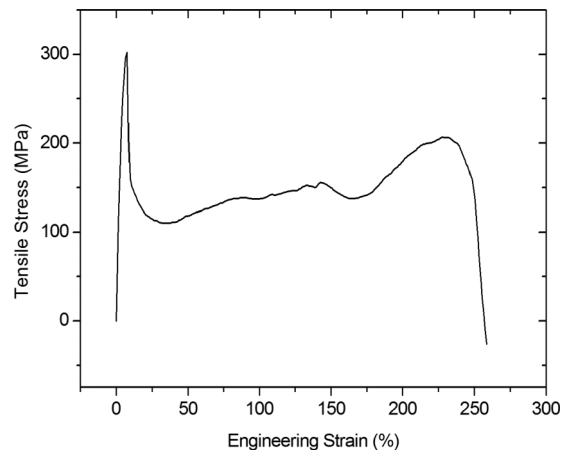

FIG. 2. Stress-strain curve of the tensile deformations.

are colored by their coordination numbers. The coordination number of a bead is the number of its neighbors within the force-field (LJ potential) cutoff distance. Therefore, the higher the coordination number is, the more densely packed the beads are. In the color scheme adopted in Fig. 3, more reddish means higher coordination number, while more blue means lower coordination number. Following this color scheme, it is easy to visualize the cavities in the simulation cell. These cavities grow with increasing strain, mainly by elongating in the direction of loading. During cavity growth and elongation, the stress-strain curve shows a rather mild strain hardening between 20% and 200% strain. As shown in Fig. 3(b), cavities grow both longitudinally and laterally. Such a weak hardening behavior is a result of the network strands realigning themselves in the loading direction, which yields large strain without significant stress increase. After about 200% strain, most of the network strands are taut in the loading direction and the entire simulation cell is changed to a network of ligaments and cavities [see the snapshot in Fig. 3(c)]. Further increasing the strain leads to bond stretching in the ligaments, which thus increases the stress. Eventually, some of the bonds are broken, creating a cascade of bond failure that leads to the final failure of the material by rapid scission of a large number of strands at about 230% strain [see Figs. 3(d) and 3(e)]. Failure is seen as breakage of the ligaments.

Another interesting observation is the network of strands connecting the inner walls inside the cavities. An enlarged view of a typical cavity is shown in Fig. 4. It can be seen that within the cavity the network strands have been stretched from their initial close-packed states to taut conformations. The taut network strands bear high stress and break upon further stretching, as will be discussed in detail later in this article.

B. Yielding criterion

In glassy polymers, both shear and dilatational stresses contribute to yielding. Generally speaking, higher hydrostatic pressure leads to higher effective yield strength. To account for the effects of hydrostatic pressure on the yielding behavior of glassy polymers, the pressure-modified von Mises yield criterion [21] is often used, which states that yielding occurs when the von Mises (octahedral shear) stress τ_h reaches a
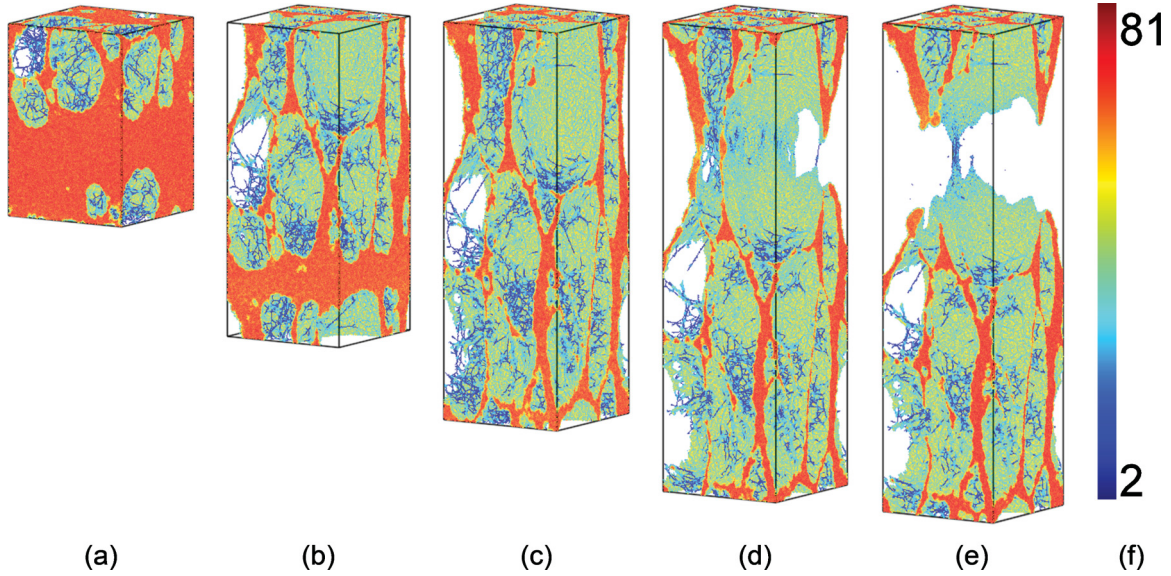
FIG. 3. (Color online) Snapshots of the deformation sequence. Strains are (a) 45%, (b) 140%, (c) 200%, (d) 255%, and (e) 260%. (f) shows the color bar. Snapshots are made by AtomEye [20]. The dark gray corresponds to the network strands connecting the inner wall of the cavities, the medium gray corresponds to the matrix surrounding the cavities, and the light gray corresponds to the boundary of the cavities.

threshold value τ_Y^p, i.e.,

$$\tau_h = \tau_Y^p \equiv \left(\tfrac{2}{3}\right)^{1/2}\tau_Y + \alpha p, \qquad (4)$$

where τ_Y is the yield strength under pure shear, p is the hydrostatic pressure, and α is a dimensionless parameter accounting for the effects of p. The octahedral stress can be expressed as a function of the principal stresses σ_1, σ_2, and σ_3,

$$\tau_h = \tfrac{1}{3}\sqrt{(\sigma_1 - \sigma_2)^2 + (\sigma_1 - \sigma_3)^2 + (\sigma_2 - \sigma_3)^2}. \qquad (5)$$

For a given material, the value of τ_Y can be obtained by conducting a pure shear test. To obtain the value of α,
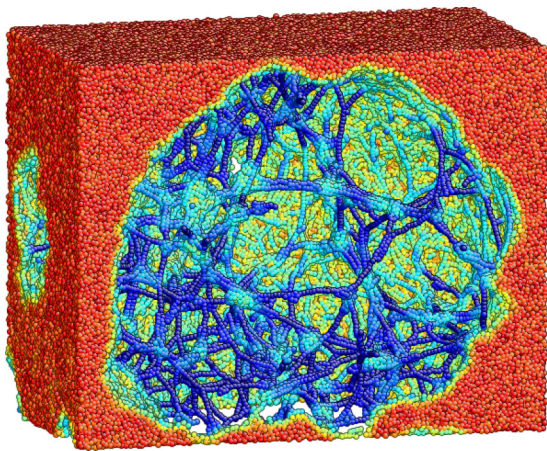

FIG. 4. (Color online) Enlarged view of one cavity in the simulation cell at 45% of strain. Beads are colored according to coordination number and the corresponding color map is the same as that shown in Fig. 3. The dark gray corresponds to the network strands connecting the inner wall of the cavities, the medium gray corresponds to the matrix surrounding the cavities, and the light gray corresponds to the boundary of the cavities.

multiaxial tests are needed. Such experiments are often time consuming and expensive.

In this work, the values of τ_Y and α for the material considered here were obtained by simulating the yield behavior under pure shear and several other multiaxial loading conditions using the CGMD simulations. Several examples of these loading conditions are illustrated in Fig. 5. The strain rate used in these studies was either 10^8 s^{-1} or a fraction of it. In the directions that the stress was controlled, the Nosé-Hoover barostat was used to maintain zero traction.

To compute the pressure-modified yield strength τ_Y^p, the stress-strain curve σ_1 versus ε_1 in the vertical direction (see Fig. 5) was computed for various loading conditions. Let σ be the normal stress in the major loading direction and ε be the corresponding normal strain. At the point when $\sigma = \sigma^{\max}$, where $\sigma^{\max}$ is the maximum on the σ versus ε curve, the corresponding three-dimensional state of stress was used to compute the von Mises stress τ_Y^p according to (5) and the pressure p according to $p = -(\sigma_1 + \sigma_2 + \sigma_3)/3$. The τ_Y^p so computed as a function of p is plotted in Fig. 6 using the solid squares. It is seen that the von Mises stress at yielding indeed depends on the hydrostatic pressure p. Higher hydrostatic pressure leads to higher yield strength. By fitting the τ_Y^p versus p relationship in Fig. 6, the values of τ_Y and α can be obtained. It is seen that $\tau_Y = 61.9$ MPa and there are two distinctive values of α, namely, $\alpha = 0.124$ for $p > -275$ MPa and $\alpha = 0.334$ for $p < -275$ MPa. Observations of the microstructure evolution at yielding further reveal that yielding is primarily due to shear for $p > -275$ MPa, while for $p < -275$ MPa, yielding is primarily due to cavitation. Values of α reported in the literature [5] range from 0.09 to 0.15, depending on the bond potential parameter and polymer chain length. Our results for α are in line with these literature values.

We note that the process described above to compute τ_Y^p is somewhat different from that used in [5] where τ_Y^p is taken as $\tau_h^{\max}$, where $\tau_h^{\max}$ is the maximum value of the τ_h
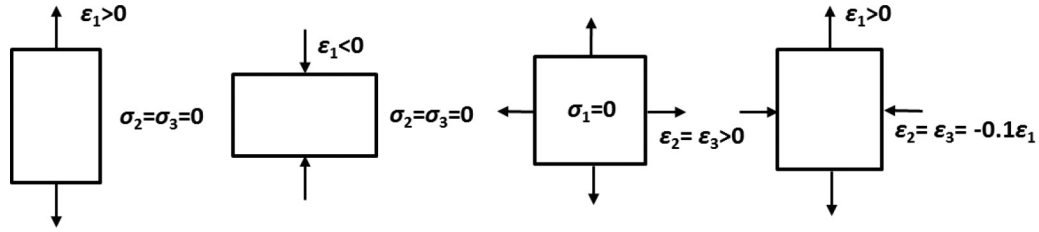
FIG. 5. Examples of the loading conditions considered.

versus ε curve. In all the loading cases considered in our studies, we found that the strain ε at which $\sigma = \sigma^{\max}$ is always less than or equal to the strain ε at which $\tau_h^p = \tau_h^{\max}$. Therefore, we believe that using the stress state at $\sigma = \sigma^{\max}$ to compute τ_Y^p as described in the previous paragraph is more appropriate, since the loading is displacement controlled.

C. Cavity formation and growth

An important aspect of the deformation and failure mechanism of the studied epoxy-based thermoset is cavity nucleation and growth. One may speculate that cavities appear at the locations where the epoxy has a less interconnected network in its initial configuration. In order to find out whether the formation of cavities is related to the polymer network's cross-linking structure, the spatial distribution of the cross-links is studied. The cross-links are defined as the beads having at least three strands reaching out and linking to other such beads in the cross-linked polymer network. We find that the cross-links in our simulations cell are rather uniformly distributed, indicating that the cross-linked polymer network does not have inherent inhomogeneity that could lead to the cavity nucleation sites upon loading. One may then conclude that the locations of cavitation sites are not related to the initial cross-linked network structure. As a further confirmation, we found that if the tensile simulation starts at different equilibrium states of the same initial cross-linked network structure, the locations of cavitation sites are different, an indication that the initiation sites of cavities are not intrinsically related to the initial cross-linked network structure.

Furthermore, we found that regardless of the statistical difference in the initial cross-linked network structure and the difference in the cavity nucleation sites, the stress-strain curve remains the same so long as the conversion is the same. This implies that the nucleation of cavities has a random nature. However, the cavitation processes for materials with the same conversion are statistically similar, so the resulting stress-strain curve is the same.

After the cavities are initiated, they grow with increasing deformation. To differentiate cavities from their surrounding matrix materials and to track the evolution of the cavities, the entire simulation cell is divided into Voronoi cells by using each bead as the center of the Voronoi cell. The volume of the ith Voronoi cell will be denoted by V_i^{Voro}, so the total volume of the simulation cell is $V = \sum_i V_i^{\text{Voro}}$. During deformation, a cavity is considered nucleated when the volume of a Voronoi cell becomes greater than a threshold value V_{th}^{Voro}. Clusters of beads with Voronoi cell volume larger than V_{th}^{Voro} are shown in Fig. 7, where the threshold volume V_{th}^{Voro} is determined such that the mass density of the cavity is less than 3% of the mass density of the surrounding matrix.
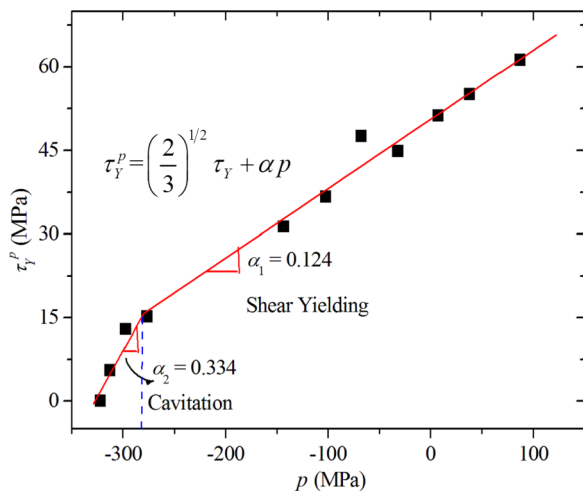

FIG. 6. (Color online) Pressure-modified von Mises yield strength versus hydrostatic pressure.
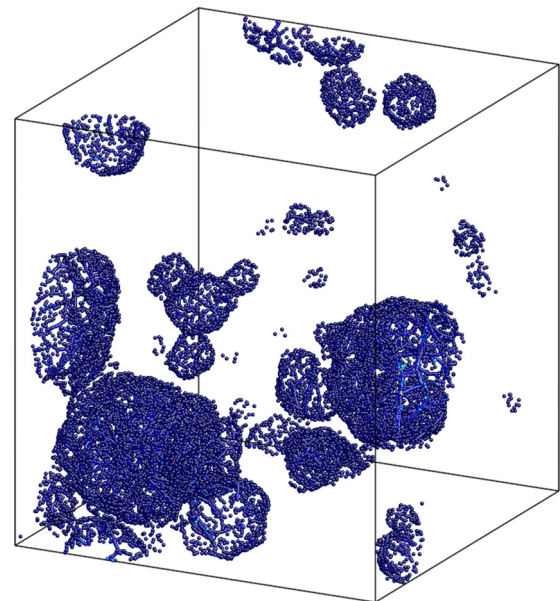

FIG. 7. (Color online) Visualization of clusters of beads with Voronoi cell volume larger than a threshold volume. Beads are colored according to their Voronoi cell volumes.
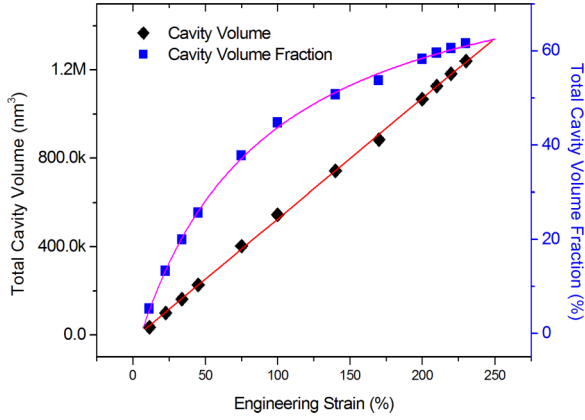
FIG. 8. (Color online) Total cavity volume (black diamonds) and the cavity volume fraction (blue squares) versus axial strain in the loading direction.

The total volume of the cavities in the simulation cell is given by

$$V^c = \sum_i V_i^{\text{Voro}} \bigg|_{V_i^{\text{Voro}} > V_{th}^{\text{Voro}}}. \tag{6}$$

In Fig. 8 the total volume and the volume fraction of the cavities are plotted as functions of the axial strain in the loading direction. The symbols are from our CGMD simulations and the solid lines are the best fits of the data. It can be seen from the plot that the total cavity volume increases linearly with increasing strain throughout the deformation process and the ultimate failure of the material occurs when the volume fraction of cavities reaches about 60%. Although not shown here, observations of the cavity evolution indicate that the increase of V^c is due to both the expansion of the already nucleated cavities and the continuous nucleation of additional cavities with increasing loading.

It follows from the data shown in Fig. 8 that $V^c = \alpha \varepsilon_1$, where ε_1 is the engineering strain in the loading direction and $\alpha = 533\,333$ nm^3 is the slope of the straight line in Fig. 8. Since the deformation is a uniaxial strain and the initial simulation box is a cube of dimension L, the total volume of the simulation box during the uniaxial strain deformation is $V = (1 + \varepsilon_1)L^3$. Therefore, the cavity volume fraction is given by $f_c = V^c/V = \alpha \varepsilon_1/(1 + \varepsilon_1)L^3$ (see the blue squares in Fig. 8). It is interesting to compute the ratio of the total cavity volume and the volumetric change of the simulation cell $V^c/(V - L^3) = \alpha/L^3 = 0.87$. This means that 87% of the volumetric change of the simulation cell is due to cavitation. The volumetric change of the matrix accounts for only 13% of the total volumetric change of the simulation box. In other words, during uniaxial strain, the deformation is primarily accommodated by voiding.

D. Network strand scission

As mentioned in Sec. III A, polymer network strands are continuously pulled taut and may break if bonds reach the cutoff length given by the potential. To quantitatively study this process, we measured the distances between cross-links. As described in Sec. III C, cross-links are those beads having
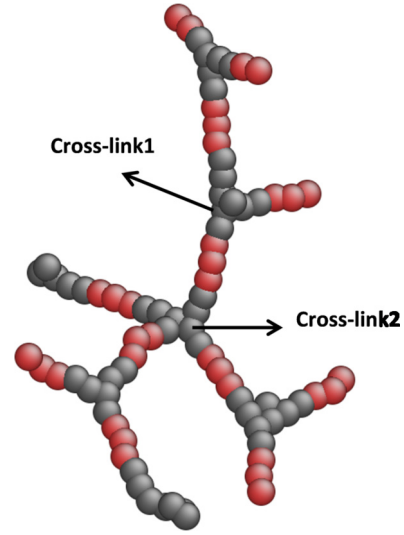

FIG. 9. (Color online) Illustration of one piece of cross-linked polymer network with two linked cross-links marked.

at least three strands reaching out and linking to other such beads in the cross-linked polymer network. In Fig. 9 a pair of such linked cross-links is shown. For convenience, we use d to denote the distance between the two cross-links and l to denote the equilibrium length of the strands connecting them. In the initial configuration, $d/l < 1$ for most cross-links, since strands are mostly coiled in the undeformed configuration. As deformation increases, d approaches l when strands are pulled taut. Thus the ratio $\mathcal{R} = d/l$ gives a good measure of the degree to which strands are pulled taut. The probability distribution of $\mathcal{R}$ was studied for various deformed configurations and is plotted in Fig. 10. It is evident that $\mathcal{R}$ approaches 1.0 as the overall strain increases. In the initial configuration, the peak of the $\mathcal{R}$ distribution is centered around $\mathcal{R} = 0.47$. This peak shifts toward the right and becomes lower as deformation proceeds and eventually vanishes. In the meantime, a second peak emerges at $\mathcal{R} = 0.8$ after the strain reaches 45%. As the strain increases further, this second
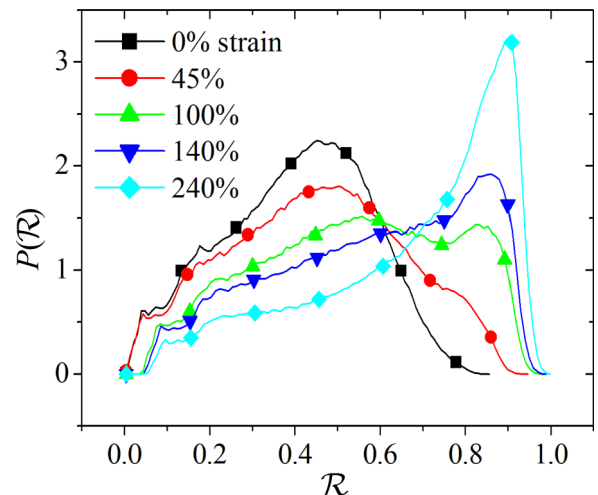

FIG. 10. (Color online) Probability distribution of $\mathcal{R}$ at various strain levels.
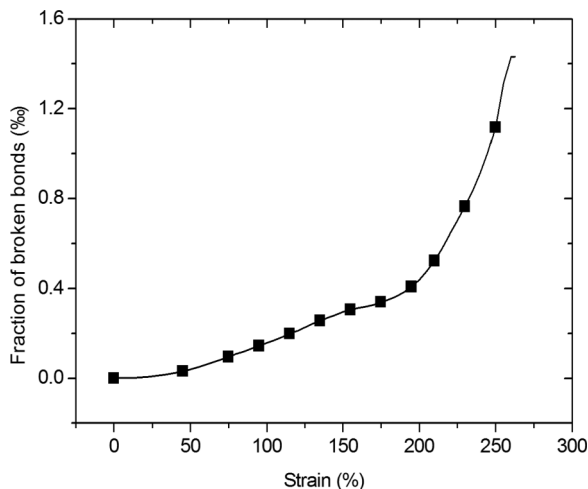
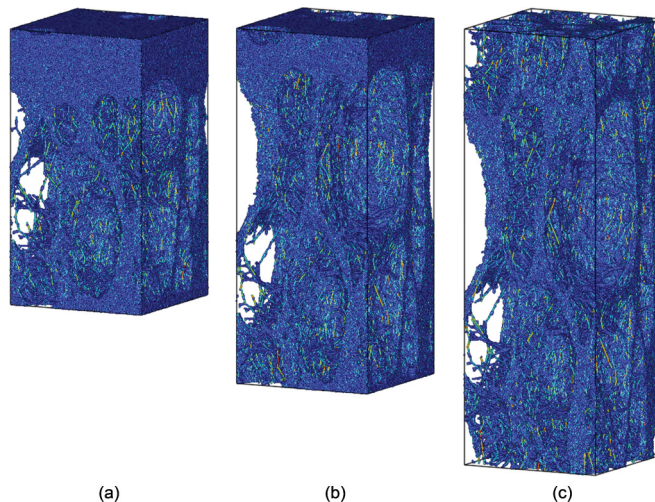FIG. 11. Fraction of broken bonds versus strain.

FIG. 12. (Color online) Atomic configurations with beads colored by their atomic stress along the loading direction. The corresponding strains are (a) 90%, (b) 145%, and (c) 200%. The light gray corresponds to higher stress and the dark gray corresponds to lower stress.

peak shifts to $\mathcal{R} = 0.9$ at about 240% strain, with its height significantly increased. These trends clearly demonstrate that strands are continuously being pulled from close-packed to linear states.

A covalent bond may break when strands are stretched longer than their maximum length defined by the bond potential (2). Figure 11 plots the fraction of broken bonds (among a total of $\sim 8 \times 10^6$) with respect to the applied uniaxial strain. It is evident from the plot that the number of broken bonds per unit increment of strain increases significantly beyond a strain of $\sim 150\%$. This finding is consistent with the data shown in Fig. 10 in that it is only after most of the strands are extended to taut configurations that the rate of bond breaking increases significantly. Also, a strain of $\sim 150\%$ coincides with the starting point of the strain hardening regime of the stress-strain curve, as discussed in Sec. III A, which indicates that the strain hardening is indeed accompanied by rapid scission of a large number of strands. Further investigation of the stress distribution confirms this conclusion. In Fig. 12, where beads are colored by their atomic stress along the loading direction, it is shown in Fig. 12(c) that the chains bearing high stress (chains with lighter color) can be found throughout the entire simulation box, while in Figs. 12(a) and 12(b) they are localized around the cavities. Therefore, many more covalent bonds are expected to break in the strain hardening process.

E. Comparison with thermoplastic glassy polymers

We have shown that, in thermoset polymers such as cross-linked epoxy under high hydrostatic tensile stress, yielding occurs via cavitation. Molecular dynamics studies of thermoplastic glassy polymers [10,15] reported a similar phenomenon of cavitation and, accordingly, a drastic stress relaxation after yielding in the stress-strain behavior. In other words, under high hydrostatic tensile stress, thermosets and thermoplastics both yield through cavitation.

After the stress relaxation, the stress in thermoplastic polymers stays on a plateau value, i.e., the drawing stress, and the range of this plateau regime, measured by the stretch ratio L_z/L_z^0, is roughly 4 according to the results presented

in [10,15]. It is well understood that craze grows during this process through void expansion and chain disentanglement. Stable crazes are characterized by a well-defined network of interconnecting voids and fibrils [15]. Although cavity growth also occurs during the postyielding deformation process of the cross-linked thermosets, the behavior is different in that postyielding stress increases instead of staying at a constant value. This is due to the continuous orientating and scission of rather short polymer network strands, as has been demonstrated in Sec. III D (Figs. 10 and 11). As can be seen from Fig. 4, inside the cavities the network strands have been stretched from their initial close-packed states to taut conformations. Thus growth of the cavities causes more strands to change from a coiled state to a linear state.

In thermoplastics, crazes fail through disentanglement for shorter chains or chain scission for long chains ($N \geqslant 2N_e$) [10]. In thermosets, neither of these two mechanisms plays a role. Instead, it is the scission of permanently cross-linked, much shorter chains, which occurs significantly more rapidly prior to failure. In [10] the stretch ratio L_z/L_z^0 required from the end of stress plateau to the ultimate failure is roughly 3 for thermoplastics, while the value is less than 1 for the thermoset epoxy studied in this paper. In other words, the highly cross-linked network structure makes thermosetting polymers more brittle than thermoplastic polymers. This is because the chemically cross-linked network forbids chain disentanglement and leads to breakage of chains and thus brittle failure of the material.

F. Comparison to experimental observations

It has been found in experimental studies that in epoxies localized plastic deformations usually occur within a very narrow band measured over several hundred nanometers [1–4]. In both crazing [1–3] and dilatation bands [3,4], it was observed that the crack tip consists of parallel bands of coarse fibrils bridging the crack surfaces and cavities in between. This

resembles our simulated deformed configurations in which stretched ligaments are separated by cavities. Our simulation results reveal the detailed microstructure and quantitative aspects of the localized plastic deformation, including stretch ratio, strength, and cavity volume fraction, which are not easily accessible through experiments. Therefore, they provide valuable information for continuum-mechanics-based modeling of fracture of thermosetting polymers.

IV. CONCLUSION

In the current investigation, large-scale MD simulations based on a CG model were conducted to study the deformation and failure mechanisms of an epoxy molding compound. The CG potential was developed based on matching key thermomechanical properties of the epoxy molding compound. The cross-linked network structure of the epoxy was built by running MD simulations of polymerization from the mixture of monomers. Major findings of the CGMD simulations are as follows.

(a) We found that yielding in the epoxy molding compound is caused by cavitation under high hydrostatic tension. At low hydrostatic tension or compression, yielding is caused by shear. Such yielding behavior can be described by the pressure-modified von Mises yield criterion. Through extensive numerical simulations, we obtained the material parameters in the pressure-modified von Mises criterion for the epoxy considered here.

(b) Cavities nucleate randomly and grow under increasing load. It was found that cavitation accounts for much (87%) of the volumetric change during the uniaxial strain deformation. The sample fails when the cavity volume fraction reaches $\sim$60%.

(c) Polymer strands in the network are continuously stretched to linear states and broken in the postyielding strain hardening process. When most of the strands are stretched to their taut configurations, the material shows rapid scission of a large number of strands within a short range of strain, which eventually leads to fracture.

(d) The simulation results show that the thermosetting polymers, such as cross-linked epoxy, are much more brittle than glassy thermoplastic polymers. Such brittleness is attributed to the chemically cross-linked network of very short chains, which forbids chain disentanglement.

The above findings provide valuable insights into the localized plastic deformation of thermosetting polymers. Future work based upon them may lead to atomistic-to-continuous multiscale modeling frameworks for cracking in thermosetting polymers.

[1] R. J. Morgan and J. E. O'Neal, J. Mater. Sci. **12**, 1966 (1977).

[2] H. J. Sue *et al.*, J. Mater. Sci. Lett. **12**, 1463 (1993).

[3] H. J. Sue *et al.*, in *Toughened Plastics II*, edited by C. K. Riew and A. J. Kinloch, Advances in Chemistry Series 252 (American Chemical Society, Washington, DC, 1996), p. 161.

[4] H. J. Sue *et al.*, J. Polym. Sci. Polym. Phys. **33**, 2003 (1995).

[5] J. Rottler and M. O. Robbins, Phys. Rev. E **64**, 051801 (2001).

[6] J. Rottler and M. O. Robbins, Phys. Rev. E **68**, 011507 (2003).

[7] R. S. Hoy and M. O. Robbins, Phys. Rev. Lett. **99**, 117801 (2007).

[8] R. S. Hoy and M. O. Robbins, Phys. Rev. E **77**, 031801 (2008).

[9] J. Rottler and M. O. Robbins, Phys. Rev. Lett. **89**, 195501 (2002).

[10] J. Rottler and M. O. Robbins, Phys. Rev. E **68**, 011801 (2003).

[11] J. Rottler, S. Barsky, and M. O. Robbins, Phys. Rev. Lett. **89**, 148304 (2002).

[12] M. J. Stevens, Macromolecules **34**, 2710 (2001).

[13] M. Tsige, C. D. Lorenz, and M. J. Stevens, Macromolecules **37**, 8466 (2004).

[14] M. Tsige and M. J. Stevens, Macromolecules **37**, 630 (2004).

[15] M. Panico, S. Narayanan, and L. C. Brinson, Model. Simul. Mater. Sci. Eng. **18**, 055005 (2010).

[16] S. R. Yang and J. M. Qu, Polymer **53**, 4806 (2012).

[17] S. Yang, Z. Cui, and J. Qu, J. Phys. Chem. B **118**, 1660 (2014).

[18] C. D. Lorenz, M. J. Stevens, and R. P. Wool, J. Polym. Sci. Polym. Phys. **42**, 3333 (2004).

[19] J. Kennedy and R. Eberhart, *Proceedings of the IEEE International Conference on Neural Networks* (IEEE, Piscataway, 1995).

[20] J. Li, Model. Simul. Mater. Sci. Eng. **11**, 173 (2003).

[21] R. Raghava, R. Caddell, and G. Y. Yeh, J. Mater. Sci. **8**, 225 (1973).